Vacuum swing adsorption process for post-combustion carbon capture with 3D printed sorbents: Quantifying the improvement in productivity and specific energy over a packed bed system through process simulation and optimization

Shreenath Krishnamurthy

Department of Process Technology, SINTEF Industry, Forskningsveien 1, Oslo 0373, Norway

HIGHLIGHTS

- Pellets vs. 3D printed amino silane sorbent in a VSA cycle.
- 3D printed sorbent: 2.35 x Productivity.
- UTSA-16 sorbent performs better than amino silane sorbent.

ARTICLE INFO

ABSTRACT

This fully computational work is dedicated to the simulation and optimization of a 6-step vacuum swing adsorption (VSA) process to study the performance of a 3D printed silica sorbent grafted with amino silane. The performance of the 3D printed sorbent was compared with a representative packed bed. Rigorous optimization showed that that it was possible to achieve 2.35 times improvement in productivity with a VSA process containing a 3D printed sorbent than the one using pellets. The minimum specific energy values were found to 1.06 and 1.19 MJ/kg CO_2 captured for the 3D printed sorbent and the packed bed respectively.

1. Introduction

Climate change has been the subject of debate in the recent years and this has been attributed to the enhanced greenhouse effect caused by CO_2 emissions from industries, power plants and transportation (IPCC, 2018). Over the last few years, the scientific community has been exploring technologies using solvents (Kiani et al., 2020; Wanderley et al., 2020), membranes (Lei et al., 2020; Liu et al., 2020), and solid sorbents (Dhoke et al., 2021; Farmahini et al., 2021) for capturing the CO_2 from various sources with the aim of storing the CO_2 in geological formations or for the production of valuable chemicals.

The research focus on the adsorption technology using solid sorbents can be classified into two major categories 1. Development of novel adsorbents in the context of CO_2 capture like metal organic frameworks (MOFs) (Hu et al., 2019), Zeolitic imidazolate frameworks (ZIFs) (Yang et al., 2020), covalent organic frameworks (COFs) (van der Jagt et al., 2021) etc. and 2. Process simulation and

optimization of cyclic adsorption processes using the isotherm data of commercially available and novel adsorbents. A major challenge with respect to the implementation of CO_2 capture to large emission sources like power plants is the large volumes of CO_2 emitted and capturing such large volumes requires a large footprint. For an economically attractive capture system, the footprint must be as small as possible. The reduction in footprint can be achieved by fast cycling between the adsorption and desorption steps and operating the process with high feed flowrates. Traditionally, adsorption separation processes are designed with packed bed systems, in which adsorption columns are packed with adsorbent beads or extrudates. The down side with pelletized sorbents is that the pressure drop across the columns would be significant at high flowrates and hence would increase the energy consumption (Rezaei and Webley, 2010). Repeated pressurization and depressurization can also increase the attrition in the adsorbents. To overcome these disadvantages switching from pelletized adsorbents to structured sorbents like hollow fibres, laminates, monoliths etc is recommended. Through a combination of theoretical analysis and experimental studies, Ruthven and Thaeron (Ruthven and

E-mail address: Shreenath.Krishnamurthy@sintef.no

Nomenclature

b_0	Affinity coefficient of the dual-site Langmuir isotherm for sites 1 and 2	q_i^*	Equilibrium solid phase concentration at saturation (mol/m^3)
C_T	Total gas phase concentration (mol/m^3)	R	Gas constant (J/mol/K)
c_i	Gas phase concentration of component i (mol/m^3)	r_i	Column internal radius (m)
C_{pg}	Specific heat capacity of the gas mixture (J/kg K)	r_0	Column external radius (m)
C_{pa}	Specific heat capacity of the adsorbed phase (J/kg K)	r_p	Pellet radius (m)
C_{ps}	Specific heat capacity of the adsorbent (J/kg K)	T	Temperature inside the column (K)
C_{pw}	Specific heat capacity of the column wall (J/kg K)	T_W	wall temperature (K)
D_L	axial dispersion coefficient (m^2/s)	T_a	Ambient temperature (K)
ΔH	Heat of adsorption (J/mol)	t	time (s)
h_i	internal heat transfer coefficient $(W/m^2\ K)$	ΔU	Internal energy of adsorption (J/mol)
h_0	internal heat transfer coefficient $(W/m^2\ K)$	v	interstitial velocity (m/s)
k_z	Axial thermal conductivity of the gas (W/m K)	y_i	mol fraction of component i
k_w	Thermal conductivity of the wall (W/m K)	z	Axial dimension (m)
$k_{LDF\ i}$	Linear driving force coefficient (s^{-1})		
P	Total pressure in the system (Pa)	*Greek symbols*	
P_H	High pressure in the adsorption step (Pa)	ε	bed void fraction
P_L	Vacuum pressure in the counter-current evacuation step (Pa)	ρ_s	density of the adsorbent (kg/m^3)
		ρ_g	density of the gas mixture (kg/m^3)
P_{INT}	Vacuum pressure in the co-current evacuation step (Pa)	ρ_w	density of the wall (kg/m^3)
P_{ATM}	Ambient pressure (Pa)	η	vacuum pump efficient
q_i	Solid phase concentration (mol/m^3)	ϒ	ratio of the specific heats
q_s	Solid phase concentration at saturation (mol/m^3)	μ	viscosity of gas mixture (Pa s)

Thaeron, 1997) calculated the height equivalent to a theoretical plate (HETP) for a parallel passage contractor of a known layer spacing and a packed bed with pellets of the same dimension as the channel depth. They had shown that the parallel passage contractor had a lower pressure drop in comparison with the packed bed for a given number of stages. However with the same characteristic dimensions, the packed bed had a lower HETP than the parallel passage contactor. Nevertheless, at larger flowrates, the HETP is a function of the layer spacing and therefore the HETP can be lowered by choosing a smaller distance between layers. This could potentially mean that with a structured sorbent one can have a smaller unit in comparison with packed beds. Besides the favourable characteristics of good mass transfer and lower pressure drop, these sorbents also have lower attrition in comparison with pellets (Grande et al., 2006). This means that there is a lower possibility of the adsorbent crumbling due to repeated pressurization and depressurization, thereby, reducing the frequency of sorbent replacement.

Although structured sorbents have been in existence for some time, very few studies have explored their performance in a cyclic adsorption process for CO_2 capture. In one of the studies, Rezaei et al., (Rezaei et al., 2010) showed through process simulations that monoliths containing zeolite films exhibit a higher productivity than packed bed systems at fast cycles (<15 s) due to improved mass transfer in a 3-step vacuum swing adsorption (VSA) process. Plaza et al., (Plaza et al., 2017) evaluated the performance of a honeycomb carbon monolith in a TSA process. Their work considered a flue gas stream containing 13.6% CO_2, 10.2% H_2O balanced by N_2. The TSA process had three basic steps, adsorption, rinse and product step. With 24 columns operating continuously, the cycle was able to achieve 95% purity and >85% recovery from the aforementioned stream coming out of a representative 800 MW power plant. The specific energy consumption values for two different sets of operating conditions were 4.89 and 3.89 MJ thermal energy/kg of CO_2 captured. The corresponding productivity values were 1.17 mol/m^3 ads s and 1.34 mol/m^3 ads /s. The authors had also shown that with a faster kinetics, the productivity can be

improved to 1.74 mol/m^3 ads s and the energy consumption lowered to 2.89 MJ/kg. A 3-bed 7-step VSA cycle was studied by Mohammedi in the context of post-combustion carbon capture from a 15.9% dry CO_2 feed (Mohammadi, 2017) using a Zeolite 13X sorbent. Through a combination of experiments and simulations, it was shown that the structured zeolite 13X sorbent was able to achieve 90% purity and recover 90% of the CO_2 fed. Zhao et al., (Zhao et al., 2019) compared performance of a hybrid monolith containing zeolite ZSM-5 and carbon and an activated carbon monolith in a VSA and electric swing VSA (EVSA) process through means of experiments and process simulations. In their study, they had observed that the VSA process was able to achieve 23% purity and 70% recovery, while the EVSA process showed a purity of about 33% and the recovery was about 72%. Furthermore, the authors had observed that the VSA process had an energy consumption of 0.25-0.3 MJ/kg CO_2 captured, while the EVSA process was more energy intensive with energy consumption values ranging from 2-6 MJ/kg of CO_2 captured More recently, Sharma et al., (Sharma et al., 2020) showed that an adsorption process with a monolithic sorbent achieved nearly 95% purity and 90% recovery in an 8-bed 14-step vacuum pressure swing adsorption (VPSA) cycle for CO_2 capture from a steam methane reformer flue gas containing 17.2% CO_2 using a NaY zeolite monolith. Correspondingly, for the same cyclic parameters and same adsorbent volume, a packed bed system achieved only 83% purity and 84% recovery due to the underutilization of the packed bed. It should be noted that these studies do not talk about any process optimization which could provide a clearer picture on the true potential of these structured sorbents. To the best of the author's knowledge, there is no published study in literature that report results from process optimization using structured sorbents and in particular, there are no studies that report energy vs productivity Pareto plots for structured sorbents. Therefore, there is indeed not much information on the productivity improvement that can be achieved when a cyclic adsorption process switches from using pellets to these structured sorbents.

The structured sorbents are produced by techniques like spinning (Lively et al., 2009), extrusion (Sakwa-Novak et al., 2016;

Regufe et al., 2018) dip coating (Chaparro-Garnica et al., 2020; Lawson et al., 2021; Wu et al., 2021) and 3D printing (Regufe et al., 2019; Middelkoop et al., 2019; Grande et al., 2020; Mendes et al., 2021). In particular, 3D printing is currently being pursued by several research groups across the globe owing to the advantages of control and flexibility with respect to the channel dimensions, channel geometry, wall thickness and the material loading in the adsorbent (Thakkar et al., 2017; Couck et al., 2018; Grande et al., 2020; Lawson et al., 2021). In a recent study from our group, a 3D printed silica grafted with amino silane was characterized for adsorption equilibrium using a commercial volumetric apparatus (Sluijter et al., 2021). Then about 12 structures were packed into a column and breakthrough experiments were performed at 3 different temperatures with a 15% CO_2 and 85% He mixture. Then a simple 3-step vacuum swing adsorption (VSA) experiment containing the following steps: Pressurization, adsorption and evacuation was carried out. The experimental data was used to validate a 1-dimensional (1D) adsorption process model. Figs. S1 and S2 show the results from the breakthrough and PSA experiments from the earlier study. In general, the simulations from the 1D process model had a good agreement with the experimental data shown in these two figures. Further, pressure drop tests also revealed that the column packed with a 3D printed sorbent had a significantly lower pressure drop (Fig. S3) than a packed bed of the same length.

The aim of this work is to study the performance of the above mentioned amino silane grafted 3D printed silica sorbent in a VSA process through means of simulations and rigorous process optimization by genetic algorithm. For this study we have chosen a 6-step VSA process containing the following steps: Adsorption, heavy reflux, co-current evacuation, counter-current evacuation, light reflux and light product pressurization. Here a dry flue gas containing 15% CO_2 and 85 % N_2 and available at 1 atm and 90 °C is considered. The specific objectives of the process optimization are the following:

1. Identify the minimum specific energy and maximum productivity values for the 3D printed sorbent for purity values > 95% and recovery values > 70%. In most published literature reporting pareto plots of VSA cycles, the recovery constraints have been fixed to > 90%. However, a recent study has shown that it is indeed possible to achieve an improved performance by reducing the recovery requirements (Maruyama et al., 2020).
2. Compare the performance of the 3D printed sorbent with a reference pellet grafted with amino silane and with other pelletized and 3D printed sorbents.

2. Adsorbent data

CO_2 adsorption isotherms on the amino silane grafted silica pellets and 3D printed sorbent were extracted from previous published study (Krishnamurthy et al., 2021b; Sluijter et al., 2021). These adsorption isotherms on the pelletized and 3D printed adsorbent are shown in Fig. 1a along with the dual-site Langmuir isotherm fits for the sake of consistency. N_2 adsorption is negligible in the amine grafted sorbent and hence it is not shown in the figure. A comparison of the adsorption isotherm with that of the pellet is shown in Fig. 1b. The CO_2 adsorption capacity is about 25% lower in the 3D printed sorbent which could possibly be attributed to the lesser amount of silica available and consequently a lower amount of amine being grafted than the pellet. Moreover, the adsorption isotherm is also more nonlinear in the case of the structured sorbent. Table 1 shows the dual site Langmuir adsorption isotherm (Eq. (1)) parameters for both the sorbents. The saturation capacities are reported in mol/m³ by multiplying with the densities shown in Table 2.
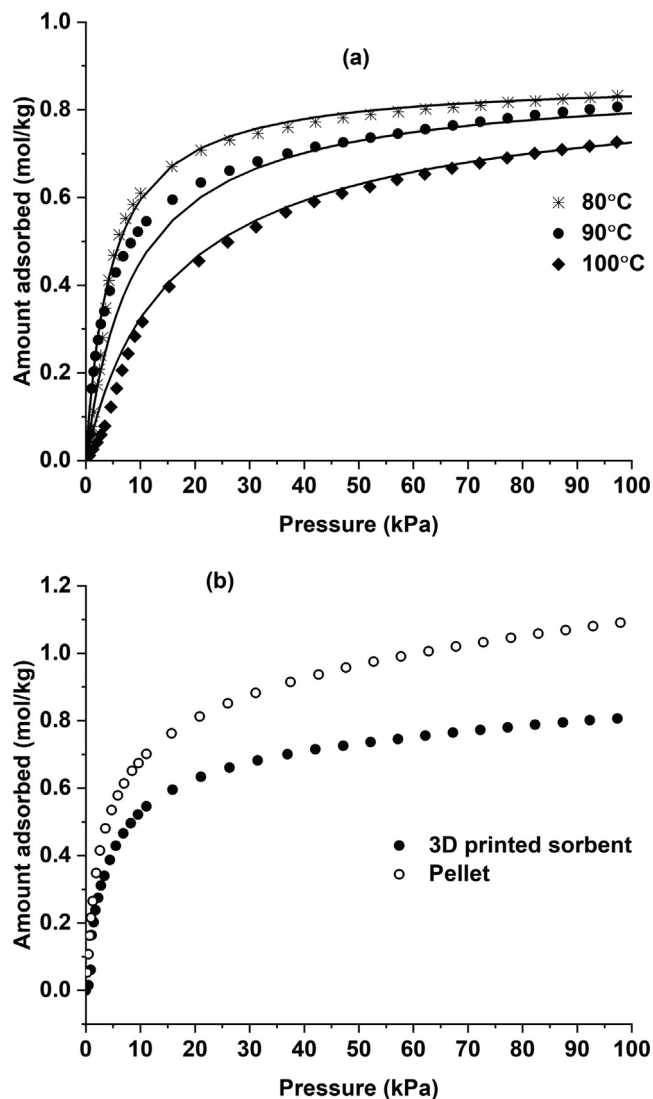
Fig. 1. (a) CO_2 isotherms in the 3D printed amino-silane sorbent and (b) comparison of CO_2 isotherms at 90 °C in the 3D printed sorbent and the reference pellet.

Table 1
CO_2 isotherm parameters for the amino silane grafted silica pellet and 3D printed silica.

Parameter	Pellet	3D printed sorbent
q_{s1}(mol/m³)	860.2	312.7
$b_{0,1}$(m³/mol)	2.74×10^{-16}	9.4×10^{-18}
ΔU_1 (kJ/mol)	−107.8	−115.6
q_{s2}(mol/m³)	521.9	263.3
$b_{0,2}$(m³/mol)	6.5×10^{-9}	5.9×10^{-8}
ΔU_2 (kJ/mol)	−46.7	−47.1

$$q_i^* = \frac{q_{s,i}^1 b_{0i}^1 e^{\frac{-\Delta U_i^1}{RT}} c_i}{1 + \sum_{i=1}^n b_{0i}^1 e^{\frac{-\Delta U_i^1}{RT}} c_i} + \frac{q_{s,i}^2 b_{0i}^2 e^{\frac{-\Delta U_i^2}{RT}} c_i}{1 + \sum_{i=1}^n b_{0i}^2 e^{\frac{-\Delta U_i^2}{RT}} c_i} \qquad (1)$$

It should be noted that in Fig. 1 the isotherms are plotted as a function of pressure, while the isotherm equation is expressed in terms of concentration. This was done to ensure dimensional consistency for the model. The kinetic constants for CO_2 adsorption were obtained from breakthrough experiments described in the previous publications respectively for the pellet and the 3D printed

Table 2
Input parameters to the process simulations. The feed temperature for both the simulations were kept at 90 °C for both the cases.

Parameter	Pellet	3D Printed sorbent
Length of column (m)	1	1
Internal diameter (m)	0.1445	0.1445
External diameter (m)	0.162	0.162
Column void fraction	0.37	0.62
Adsorbent density (kg/m^3)	1052	669.5
Adsorbent specific heat (J/kg/K)	1700	1700
Channel dimensions (mm)	Na	2.4
Channel wall thickness (mm)	Na	0.7
Pellet diameter (mm)	2.0	Na
Average pore diameter (nm)	15	78
Internal heat transfer coefficient (W/m^2 K)	0	0
External heat transfer coefficient (W/m^2 K)	0	0
Specific heat of the gas mixture (J/kg/K)	1034	1034
LDF coefficient of CO_2 (s^{-1})	1.0 x 10^6 e$^{-6415/T}$	2 × 10^8 e$^{-7255/T}$
LDF coefficient of N_2 (s^{-1})	100	100
Amount of adsorbent (kg)	43.5	16.7

sorbent (Krishnamurthy et al., 2021b; Sluijter et al., 2021). In these studies, breakthrough experiments were carried out for multiple temperatures from 70 to 100 °C. The experiments were then analysed with the non-isothermal and non-isobaric model by fitting the linear driving force coefficient and the heat transfer coefficient values. The density and porosity of the sorbent came from independent mercury intrusion experiments while the specific heat capacity values were taken from the previous study. These values are summarized in Table 2. One can see that the solid density of the pellet is higher than that of the structured sorbent, which indicates a higher amount of active sorbent material in the pellets. This also means that the porosity of the 3D printed sorbent is higher than that of the pellets. More details about the column breakthrough and volumetric experiments and the adsorbents are provided in our earlier publications (Krishnamurthy et al., 2021b; Sluijter et al., 2021).

3. 6-step VSA process

This work has employed the 6-step VSA cycle that has been studied earlier by Khurana and Farooq (Khurana and Farooq, 2016). The schematic of the 6-step VSA process is shown in Fig. 2. It contains the following steps.

1. Adsorption step: the feed is introduced into the column at high pressure (P_H) and the light product nitrogen is collected from the product end.
2. Heavy reflux step: The column is fed with the product obtained from the light reflux step. The aim of this step is to enhance the concentration of CO_2 inside the adsorption column. The duration of this step is the same as that of the light reflux step as the product from the light reflux step is completely recycled back into the column.
3. Co-current evacuation step: The column is evacuated from the product end to an intermediate vacuum (P_{INT}) to get rid of the nitrogen in the column.
4. Counter-current evacuation step: The column is evacuated from the feed end to the low pressure (P_L) to recover the CO_2 product.
5. Light reflux step: The column is evacuated from the feed end and simultaneously purged with a part of the nitrogen product from the adsorption step to remove the remaining CO_2 inside the bed. The product of this step is fully recycled back to the column to do the rinse step.

6. Light product pressurization (LPP) step: The column is pressurized from the counter-current direction with the nitrogen product of the adsorption step to high pressure P_H.

The 6-step cycle can operate at higher vacuum pressures of 0.1 bar or greater to achieve high purity and high CO_2 recovery. This is advantageous when compared with the 4-step cycle with LPP, where the product is usually recovered at 0.03 bar or less. Secondly, this cycle uses the LR step product to improve the CO_2 concentration in the column during the heavy reflux step. This is advantageous in terms of improving the productivity of the process (Khurana and Farooq, 2016). The simulation of the 6-step VSA cycle was carried out using the validated 1D adsorption process model from our previous work (Sluijter et al., 2021). The model equations are described in the next section.

4. Process model

A non-isothermal, non-isobaric model based on the following assumptions is used:

1. Axial dispersion is considered
2. No radial temperature or concentration gradients
3. Ideal gas law is valid
4. The adsorbent properties are uniform throughout the column
5. Instantaneous thermal equilibrium between gas and solid phases
6. Uniform porosity throughout the column

The model equations are a set of coupled partial differential equations, which are given below.
Component mass balance:

$$\frac{\partial c_i}{\partial t} = \frac{\partial}{\partial z}\left[cD_L\frac{\partial y_i}{\partial z} - c_i v\right] - \frac{(1-\varepsilon)}{\varepsilon}\frac{\partial \bar{q}_i}{\partial t} \tag{2}$$

By applying ideal gas law $c = \frac{P}{RT}$ Eq. (2) becomes.

$$\frac{\partial y_i}{\partial t} + \frac{y_i}{P}\frac{\partial P}{\partial t} - \frac{y_i}{T}\frac{\partial T}{\partial t} = \frac{T}{P}D_L\frac{\partial(\frac{P}{T}\frac{\partial y_i}{\partial z})}{\partial z} - \frac{T}{P}\frac{\partial(\frac{y_i P}{T}v)}{\partial z} - \frac{RT}{P}\frac{(1-\varepsilon)}{\varepsilon}\frac{\partial \bar{q}_i}{\partial t} \tag{3}$$

The overall mass balance equation is given by.

$$\frac{1}{P}\frac{\partial P}{\partial t} - \frac{1}{T}\frac{\partial T}{\partial t} = -\frac{T}{P}\frac{\partial(\frac{P}{T}v)}{\partial z} - \frac{(1-\varepsilon)}{\varepsilon}\frac{RT}{P}\sum_{i=1}^{n}\frac{\partial \bar{q}_i}{\partial t} \tag{4}$$

As mentioned earlier, the mass transfer between the gas and the solid phases was described by linear driving force approximation which is of the following form:

$$\frac{\partial \bar{q}_i}{\partial t} = k_{LDFi}(q_i^* - \bar{q}_i) \tag{5}$$

where, k_{LDFi} is the linear driving force coefficient and q_i^* is the equilibrium solid phase concentration.

The linear driving force approximation is given by.

$$k_{LDF\,i} = k_0 e^{-\frac{\Delta E}{RT}} \tag{6}$$

The values k_0 and ΔE come from binary breakthrough experiments on the pellets and the structured sorbents. These values were obtained by regressing the residual between experiments and simulations through the fitting the k_{LDF} and the heat transfer coefficient values (Krishnamurthy et al., 2021b; Sluijter et al., 2021).

The equilibrium solid concentration is defined by an extended dual site Langmuir model.

$$q_i^* = \frac{q_{s,i}^1 b_{0i}^1 e^{-\frac{\Delta U_i^1}{RT}} c_i}{1 + \sum_{i=1}^{n} b_{0i}^1 e^{-\frac{\Delta U_i^1}{RT}} c_i} + \frac{q_{s,i}^2 b_{0i}^2 e^{-\frac{\Delta U_i^2}{RT}} c_i}{1 + \sum_{i=1}^{n} b_{0i}^2 e^{-\frac{\Delta U_i^2}{RT}} c_i} \tag{7}$$

The column energy balance and the wall temperature balance equations are as follows:

$$\left[\frac{(1-\varepsilon)}{\varepsilon} \left(\rho_s C_{ps} + C_{pa} \sum_{i=1}^{n} \bar{q}_i \right) \right] \frac{\partial T}{\partial t} = \frac{K_z}{\varepsilon} \frac{\partial^2 T}{\partial z^2} - \frac{C_{pg}}{R} \frac{\partial (vP)}{\partial z} - \frac{C_{pg}}{R} \frac{\partial P}{\partial t}$$
$$+ \frac{(1-\varepsilon)}{\varepsilon} \sum_{i=1}^{n} (-\Delta H_i - C_{pa} T) \frac{\partial \bar{q}_i}{\partial t} - \frac{2h_i}{\varepsilon r_i} (T - T_w) \tag{8}$$

$$\rho_w C_{pw} \frac{\partial T_w}{\partial t} = k_w \frac{\partial^2 T_w}{\partial z^2} + \frac{2r_i h_i}{r_o^2 - r_i^2} (T - T_w) - \frac{2r_o h_o}{r_o^2 - r_i^2} (T_w - T_a) \tag{9}$$

The pressure drop across the column was described by the following equations.

$$-\frac{\partial P}{\partial z} = 3191.6 \varepsilon v_0 \tag{10}$$

$$-\frac{\partial P}{\partial z} = \frac{180}{4r_p^2} \left(\frac{1-\varepsilon}{\varepsilon} \right)^2 \mu v \tag{11}$$

Equation (10) represents the 3D printed sorbent, while equation (11) is for the packed bed. The pressure drop in Eqs. (10) and (11) is expressed as Pa/m. Therefore, the coefficient in Eq. (10) has the units of Pa s/m². The equations are similar to the earlier publications on simulation of VSA processes (Da Silva et al., 1999; Haghpanah et al., 2013; Krishnamurthy et al., 2014; Khurana and Farooq, 2016).

The model equations were converted to a dimensionless form and discretized in the spatial domain using finite volume method to obtain a system of differential algebraic equations (DAEs). The resultant system of DAEs were solved using variable order solver ode15s in MATLAB. Details about the dimensionless equations and boundary conditions are provided in the supporting information. The VSA process was simulated assuming a uni-bed approach meaning that only one column undergoes all these steps. For the 1st cycle, the column was assumed to be saturated with nitrogen at P_L and for the subsequent cycles, the initial conditions were the final conditions of the previous steps. The cycle was simulated until cyclic steady state conditions. The CSS condition was said to be satisfied if the massbalance error for five consecutive cycles was less than or equal to 0.5%. As mentioned earlier, the durations of the light reflux and rinse steps are taken to be the same, since

the entire light reflux product is recycled back to the column. Secondly, the adsorption step supplies the feed for the light reflux and the light product pressurization steps. Therefore, the durations of these two steps must be less than that of the adsorption step. The LPP step was stopped when the column reached the desired high pressure P_H.

The process performance indicators are the CO_2 product purity, CO_2 recovery, specific energy consumption and productivity. These are defined by the Eqs. (12)–(15).

$$CO_2 \text{ purity} = \frac{\text{Moles}_{CO_2, Cn-evac}}{\text{Moles}_{Total, Cn-evac}} \times 100 \tag{12}$$

$$CO_2 \text{ recovery} = \frac{\text{Moles}_{CO_2, Cn-evac}}{\text{Moles}_{CO_2, Ads}} \times 100 \tag{13}$$

$$\text{Specific energy} = \frac{\text{Energy}_{vacuum} + \text{Energy}_{compression}}{\text{Moles}_{CO_2, \text{Counter - current evacuation}}} \tag{14}$$

$$\text{Productivity} = \frac{\text{Moles}_{CO_2, Cn-evac}}{V_{ads} \times t_{cycle}} \tag{15}$$

The energy consumption by the vacuum pumps and the compressors are calculated using Eqs. (16) and (17).

$$Energy_{vacuum} = \varepsilon \pi r_i^2 \frac{\gamma}{\gamma - 1} \int_{t=0}^{t=t_{vacuum}} vP \left[\frac{1}{\eta (P(t)_{vacuum})} \left(\frac{P_{atm}}{P(t)_{vacuum}} \right)^{\frac{\gamma}{\gamma-1}} - 1 \right] dt \tag{16}$$

$$Energy_{compress} = \frac{1}{\eta} \varepsilon \pi r_i^2 \frac{\gamma}{\gamma - 1} \int_{t=0}^{t=t_{vacuum}} vP \left[\left(\frac{\bar{P}(t)_{in}}{P_{atm}} \right)^{\frac{\gamma}{\gamma-1}} - 1 \right] dt \tag{17}$$

In Eq. (16), the efficiency of the vacuum pump η is a function of pressure (Subraveti et al., 2021).

$$\eta = \frac{15.84P}{1 + 19.8P} \tag{18}$$

The efficiency of the compressor is taken to be 72% consistent with earlier published literature (Haghpanah et al., 2013; Khurana and Farooq, 2016). The pressure in equation 18 is expressed in bars.

The co-current and counter-current evacuation steps are simulated by fixing the flowrate at the column exit, thereby mimicking a constant flowrate vacuum pump. This approach has been shown to be more realistic representation of the evacuation step rather than using an exponential pressure profile (Jiang et al., 2020; Khurana and Farooq, 2019; Subraveti et al., 2021). The pressure downstream of the column i.e., at the vacuum pump inlet is fixed to be the vacuum pressure and the pressure at the column exit is then estimated from the flowrate of the vacuum pump and the downstream pressure.

5. Process optimization

The objective of the process optimization is to identify the minimum specific energy and maximum productivity values for certain target purity-recovery constraints. This is done by means of genetic algorithm, a widely used method in the adsorption process community (Fiandaca et al., 2009; Haghpanah et al., 2013; Rajagopalan et al., 2016; Krishnamurthy et al., 2021b). The 6-step VSA cycle was simulated in MATLAB and therefore MATLAB's inbuilt genetic algorithm function gamultiobj was used. The objective functions for the optimization are given below.

$$\text{Obj}_1 = \frac{\text{Specific Energy}}{100} + 10000 * \max\left(0, \text{Tol}_{\text{purity}} - \frac{CO_2 \text{ purity}}{100}\right)^2 + 10000 * \max\left(0, \text{Tol}_{\text{recovery}} - \frac{CO_2 \text{recovery}}{100}\right)^2 \tag{19}$$

$$\text{Obj}_2 = \frac{1}{\text{Productivity}} + 10000 * \max\left(0, \text{Tol}_{\text{purity}} - \frac{CO_2 \text{ purity}}{100}\right)^2 + 10000 * \max\left(0, \text{Tol}_{\text{recovery}} - \frac{CO_2 \text{recovery}}{100}\right)^2 \tag{20}$$

$\text{Tol}_{\text{purity}}$ and $\text{Tol}_{\text{recovery}}$ are the purity and recovery constraints. As mentioned earlier, the purity constraint was chosen to be > 95%, while the recovery constraints were taken to be > 70%.

The variables that affect the performance of the VSA process are called as decision variables. For the 6-step VSA process, the decision variables are the duration of the adsorption and rinse steps, the feed flow rate, the co-current and counter-current evacuation step pressures and the flow rates to the vacuum pump in the co-current and counter-current evacuation steps. The evacuation steps were complete once the column reached the desired low pressure. The upper and the lower bounds for these decision variables are provided in Table 3. A nonlinear constraint was used for the evacuation pressures ($P_{INT} \geqslant P_L + 0.02$) so that the optimizer did not choose the same pressure values for the co-current and counter-current evacuation steps, for the sake of the least energy consumption. The total simulation time was about 24–36 h in a PC containing 12 cores (with Intel(R) Xeon(R) Gold 6134 CPU, 3.20 GHz processor) for 3000 simulations (60 generation × 50 population/generation) Fig. 2.

Table 3
Bounds for decision variables for the process optimization.

Adsorbent type	Variable	Adsorption time (s)	Reflux step time time (s)	Cocurrent evacuation pressure (P_{INT})(bar)	Counter current evacuation pressure (P_L)(bar)	Feed velocity V_0 (m/s)	Co-current evacuation step pump flowrate (m³/hr)	Counter-current evacuation step pump flowrate (m³/hr)
Pellet	Lower bound	10	1	0.1	0.1	0.1	20	20
	Upper bound	300	100	0.5	0.5	2	300	300
3D printed	Lower bound	10	1	0.1	0.1	0.1	20	20
sorbent	Upper bound	200	100	0.5	0.5	5	300	300
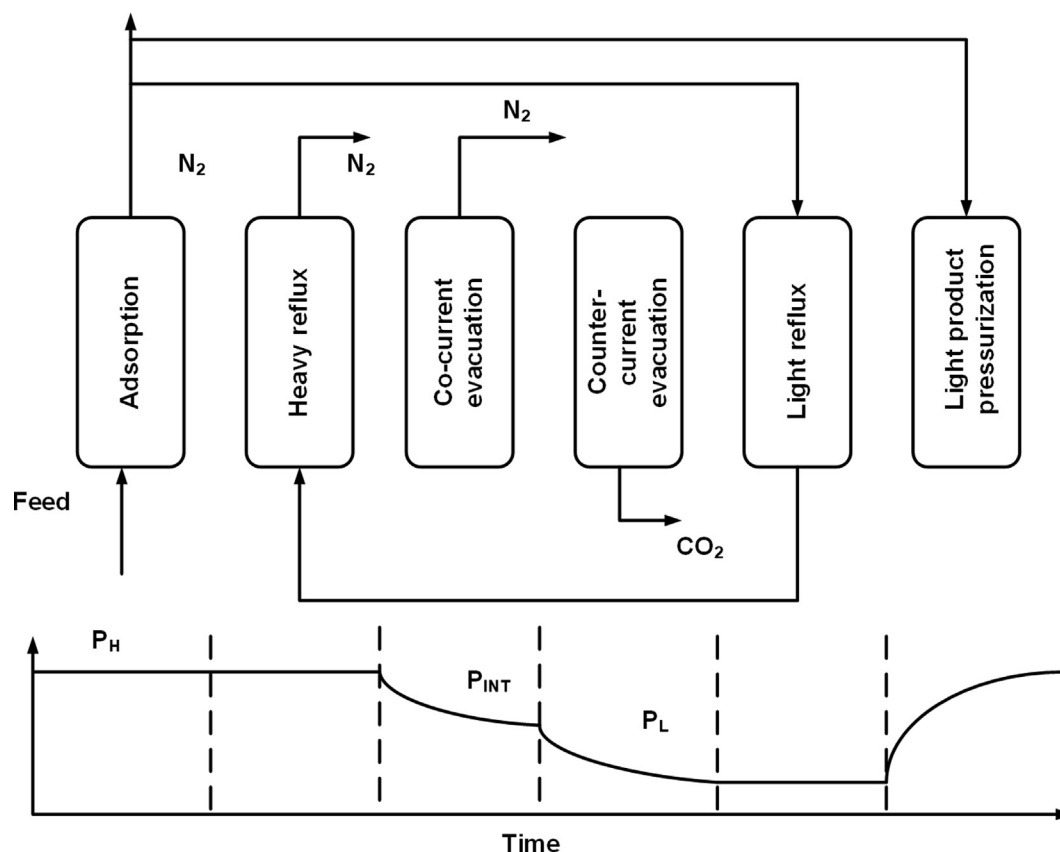
Fig. 2. Schematic of the 6-step VSA process.

6. Results and discussion

Fig. 3a shows the comparison of the specific energy vs productivity pareto for the pellet and the 3D printed sorbent. All the points on the pareto satisfy purity values of > 95%. The recovery values for the pellet were from 82.1% to 92.1%, while the 3D printed sorbent had recovery values of 79.6–87.8%. The minimum specific energy for the 3D printed sorbent is 1.06 MJ/kg of CO_2 captured while, the pellet had an energy consumption of 1.19 MJ/kg. This represents a 11% reduction in energy consumption. The maximum productivity values were 0.336 mol CO_2 captured /m^3 ads s and 0.143 mol CO_2 captured /m^3 ads s, respectively for the 3D printed sorbent and the pellets. So, the maximum productivity value was 2.35 times higher for the 3D printed sorbent. It should be noted that the energy values reported here are on an electric basis and are based on the kg of CO_2 captured.

Fig. 4 shows a comparison of the productivity vs the adsorption time, cycle time, feed flow rate and the amount of CO_2 captured for the 3D printed sorbent and the pellet. The cycle time for the 3D printed sorbent was between 74 and 92 s while the pellet had cycle times of 122–160 s. The inlet velocities (V_0) were higher for the 3D

printed sorbent due to the fast kinetics. The values the velocity varied from 0.25 to 0.35 m/s. For the pellets, the optimizer chose values between 0.16 and 0.27 m/s. This is due to the low pressure drop exhibited by the 3D printed sorbent. The combination of the faster cycle times and higher velocities contributed to an increase in productivity.

In Fig. 5, the specific energy consumption is plotted against the evacuation pressures, the total energy consumed by the vacuum pumps in the co-current, counter-current, and light reflux steps and the amount of CO_2 captured. The optimizer chose a higher evacuation pressure for the counter-current evacuation step for the pellet case than the 3D printed sorbent. This is obvious as the isotherms of the 3D printed sorbent are steeper than that of the pellets. Therefore, the energy consumed by the vacuum pump in the co-current and counter-current evacuation steps are smaller in case of the pellets than the 3D printed sorbent. However, in case of the 6-step VSA process, the light reflux step contributes to about 70% of the energy consumption. For the 3D printed sorbent, the optimizer chose 4–5 s as the duration of the light reflux step for the 3D printed sorbent, while the corresponding values for the pellet were between 15 and 20 s. The longer light reflux step duration meant that the energy consumption of the 6-step VSA cycle was higher for the pellet than the 3D printed sorbent.

In the next step, the optimization for the 3D printed sorbent was repeated by changing the lower bound of the evacuation pressure to 0.01 bar. The pareto for the 3D printed sorbent is shown in Fig. 3b and the specific energy and productivity values are shown as a function of the different decision variables in Figs. S4-S5. In this case one can see an improvement in productivity and this improvement can be attributed to the increased amount of CO_2 evacuated during the evacuation step. One can also from Fig. S4, the evacuation pressures are between 0.052 and 0.11 bar and these values are not closer to the lower bound of the evacuation step. Additionally, the reflux step durations were also between 5 and 6 s, i.e., the optimizer did not hit the lower bound. This is unlike the findings in the work of Khurana and Farooq (Khurana and Farooq, 2016), where the 6-step cycle reduced to the 4-step cycle with LPP with a light reflux step time of 1 s or less. Similar optimization was also carried out for the pellet and like the 3D printed sorbent, a significant improvement in productivity is observed. Here one can see that for some of the points, the 6-step VSA was reduced to the 4-step cycle with LPP with the reflux step duration of approximately 1 s. However, looking at Fig. S4, one can see that the evacuation pressure is 0.032 and 0.041 bar and this is lower than the values obtained from the optimization for the 3D printed sorbent. This contradicts the findings mentioned earlier in this manuscript for the simulations carried out with 0.1 bar as the lower bound. As mentioned earlier, the optimizer had chosen deeper vacuum pressures for the 3D printed sorbent when compared to the pellets. For the present case, this effect could be due to the poor fitting of the dual-site Langmuir model at pressures less than 10 kPa (0.1 bar) as seen from Fig. 1a.

The minimum specific energy and maximum productivity values for a lower bound of 0.01 bar are 1.13 MJ/kg and 0.49 mol/m^3 ads s. The corresponding values for the pellet were 1.25 MJ/kg and 0.298 mol/m^3 ads s. The improvement in the maximum productivity is now 1.46 times in comparison with the 2.35 times achieved previously. The energy consumption at the maximum productivity was around 1.93 MJ/kg for the 3D printed sorbent and about 3.2 MJ/kg for the pellet. The high energy values are consistent with the deeper vacuum pressures. It has been shown earlier by Haghpanah et al., (Haghpanah et al., 2013) and Khurana and Farooq (Khurana and Farooq, 2016), that the 4-step cycle with LPP is the most efficient cycle with respect to the energy consumption at low vacuum pressures of 0.03 bar or less. Nevertheless, low vacuum pressures such as 0.03 bar are not realistic in the industrial
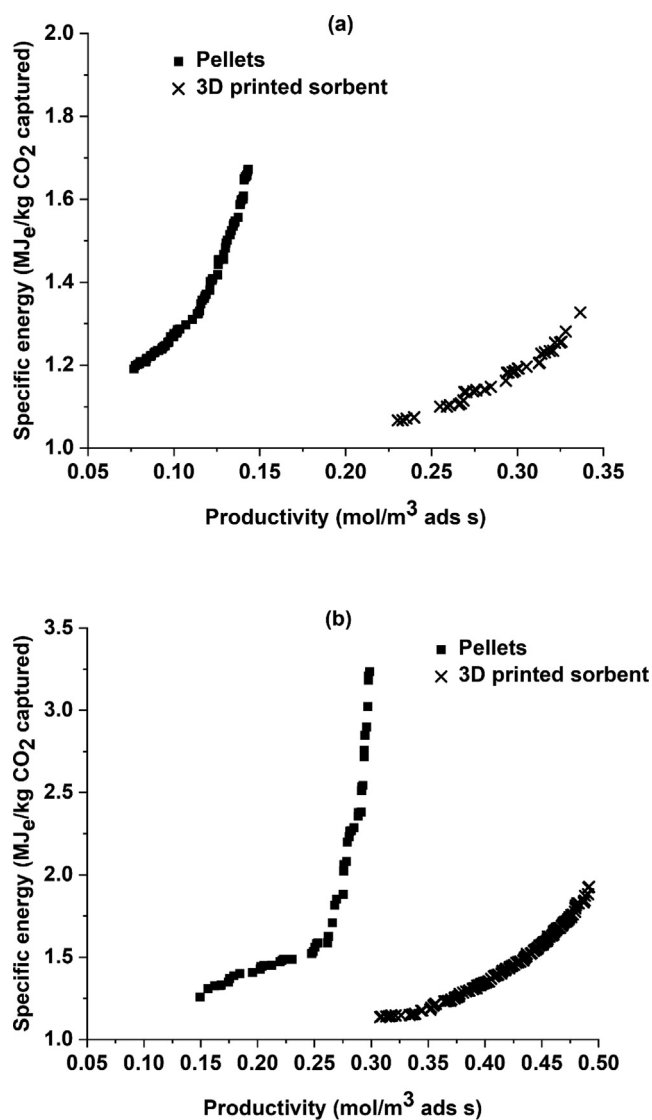

Fig. 3. Specific energy vs productivity pareto for the 3D printed sorbent and reference pellets for a lower bound of (a) 0.1 bar and (b) 0.01 bar. All points on the pareto front satisfy purity values > 95% and recovery values > 70%.
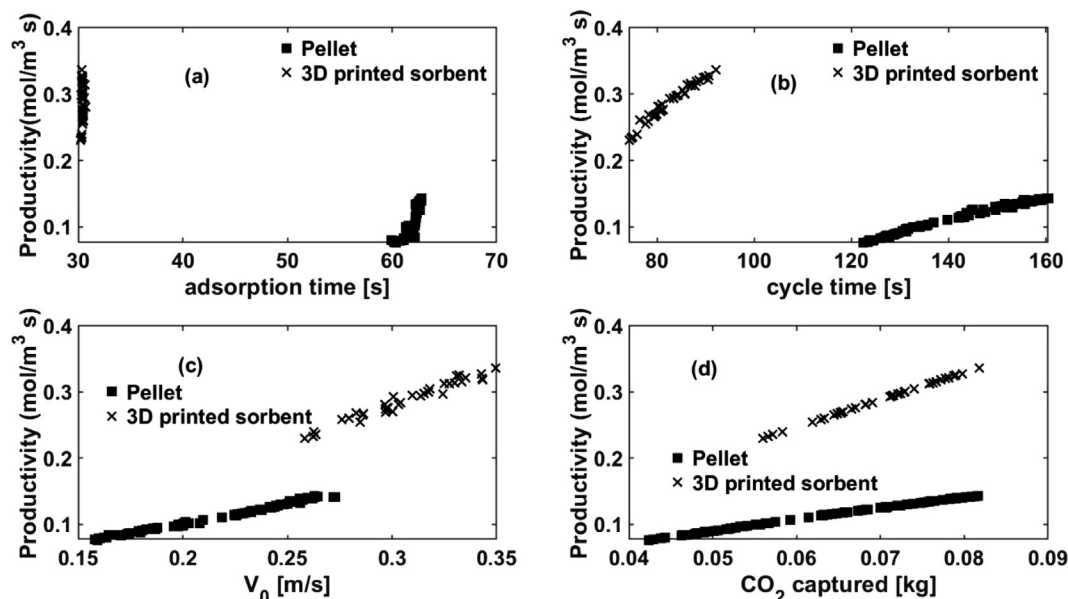
Fig. 4. Productivity vs. (a) adsorption step time, (b) total cycle time, (c) velocity of the feed and (d) CO_2 captured in the cycle.
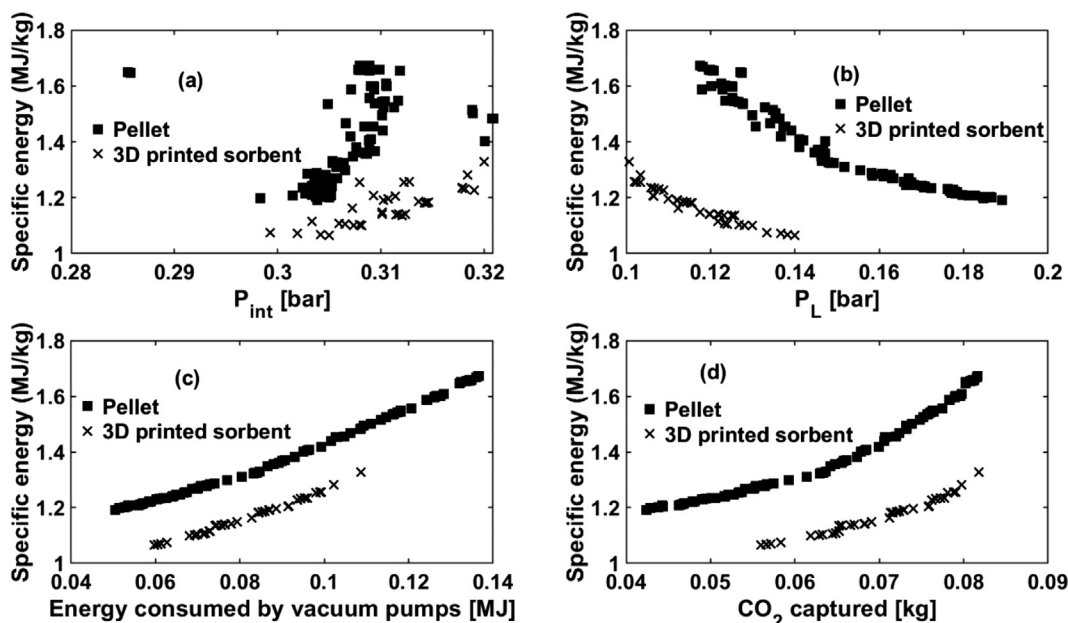

Fig. 5. Specific energy consumption vs (a) co-current evacuation step pressure, (b) counter-current evacuation step pressure, (c) energy consumed by vacuum pumps and (d) CO_2 captured in the cycle.

scale and hence the 6-step VSA process may be better suited for large scale CO_2 capture.

In the next step, the pareto fronts obtained for the amino silane grafted silica was compared with two other published 3D printed sorbents. One of them is a monolith containing multiwalled carbon nano tubes and polyethylene imine (PEI-MWCNT) (Krishnamurthy et al., 2021a) and the other one is a monolith made of UTSA-16 MOF (Grande et al., 2020). UTSA-16 in the pellet form has been studied in literature and is known to perform better than Zeolite 13X, the benchmark adsorbent for post-combustion CO_2 capture (Khurana and Farooq, 2016; Rajagopalan et al., 2016; Maruyama et al., 2020). The adsorption isotherm data for the two sorbents are taken from published literature from our group. An Arrhenius type expression was used for the k_{LDF} for the PEI-MWCNT,

whereas, for UTSA-16 the LDF expression from the work of Patton et al., (Patton et al., 2004) has been used. A comparison of the CO_2 isotherms in these sorbents is shown in Fig. 6. For the simulations with PEI-MWCNT and UTSA-16, the pressure drop across the column was described by Eq. (10).

Fig. 7 shows a comparison of the pareto fronts of the 3D printed sorbent studied in this work with two other 3D printed sorbents. While the pareto front for the PEI-MWCNT is reported at 90 °C, the pareto fronts are shown for UTSA-16 at 40 and 90 °C respectively. At 90 °C UTSA-16 and PEI had similar minimum energy consumption values of 0.77 MJ/kg, and this is 27% lower when compared with our amino silane sorbent. Even though, the amino silane grafted silica had the highest capacity, the highly nonlinear shape of the isotherm meant that this sorbent required deep vac-
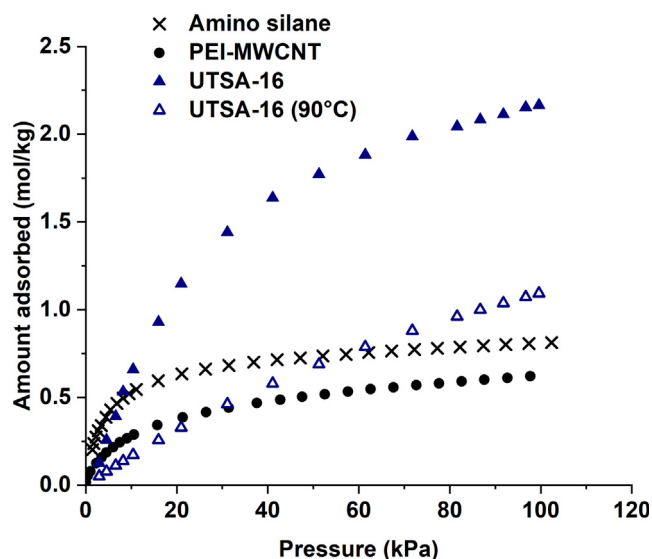
Fig. 6. CO_2 adsorption isotherms in the amino silane sorbent, PEI-MWCNT monolith and UTSA-16 monolith.

Fig. 7. Comparison of specific energy vs productivity Pareto of Amino silane with PEI-MWCNT and UTSA-16 monoliths. All points on the pareto satisfy 95% purity and 70% recovery constraints. The lower bound of the evacuation pressure is 0.1 bar.

uum pressures to recover the CO_2 as seen previously. In comparison, for the PEI-MWCNT the optimizer chose values of 0.11–0.2 bar and for UTSA-16 the values were between 0.18 and 0.2 bar. The maximum productivity values only improved marginally with the two adsorbents and the maximum productivity values were 0.35 and 0.36 mol/ m^3 ads s.

At a feed temperature of 40 °C, UTSA-16 showed even higher productivity of 0.89 mol/m^3 ads s. Lowering the temperature improved the adsorption capacity of CO_2 for UTSA-16 and it was possible to operate the cycle at higher flowrates (0.28–0.63 m/s vs 0.2–0.4 m/s), thereby improving the productivity (Fig. S6).

Table 4 shows a comparison of the maximum productivity values achieved in some of the recent literature for reference packed bed systems. While most of the cycles studied are not the same as the one shown in this work, it is evident that it is possible to achieve a higher productivity with packed beds over our 3D printed sorbent and UTSA-16 monolith. Of course, it is agreed that this comparison is not on the same basis as the cycles are different. Secondly, from the earlier discussion on the work of Ruthven and Thaeron (Ruthven and Thaeron, 1997), we saw that the HETP of the packed bed is higher than that of a parallel passage contractor of the same dimensions and the high productivity values agree with that. One may see an improvement in the HETP in reducing the channel spacing and thereby the productivity can be improved. Therefore, further work on 3D printed sorbents is necessary to identify optimum properties to achieve significant improvement in performance with these novel sorbents.

7. Conclusions

In this work, the performance of a 3D printed amino silane containing sorbent is compared with that of a reference packed system. Detailed process simulations showed that it was possible to achieve a significant improvement in productivity with the 3D printed sorbent. It should be noted that the 2.35 times improvement in productivity is reported on the basis of the adsorbent volume. If the productivity value was indeed expressed in terms of the column volume, the improvement in the maximum productivity becomes 1.4 times when the VSA process uses a 3D printed sorbent. Simulations were also carried out assuming exponential pressure decay for the evacuation steps. In this case, the improvement in productivity was around 3 times (Fig. S7). Such drastic increase was probably due to the short counter-current evacuation times and the high feed flowrates chosen by the optimizer. The use of a vacuum pump characteristic curve or a constant flowrate vacuum pump has been shown to be a good representation of the

Table 4
Specific energy and productivity values for packed bed in selected literature.

Adsorbent	Cycle and input condtions	Purity/recovery (%)	Minimum specific energy (MJ/kg)	Maximum productivity (mol/m^3 ads s)	Reference
Zeolite 13X	4-step VSA with LPP	95–90	0.59	1.5	(Nalaparaju et al., 2015)
Zeolite 13X	4-step VSA with LPP	95–90	0.55	2.5	(Khurana and Farooq, 2016)
UTSA-16	4-step VSA with LPP	95–90	0.45	2.3	(Khurana and Farooq, 2016)
Zeolite 13X	6-step VSA	95–90	0.58	4.7	(Khurana and Farooq, 2016)
UTSA-16	6-step VSA	95–90	0.47	4.28	(Khurana and Farooq, 2016)
Mg-MOF-74	4-step VSA with LPP	90–90	0.63	0.44	(Rajagopalan et al., 2016)
Zeolite 13X	4-step VSA with LPP	90–90	0.48	0.92	(Rajagopalan et al., 2016)
UTSA-16	4-step VSA with LPP	90–90	0.42	0.74	(Rajagopalan et al., 2016)
Zeolite 13X	4-step VSA with LPP	95–90	0.45	1.1	(Farmahini et al., 2018)
UTSA-16	4-step VSA with LPP	95–90	0.89	1.35	(Burns et al., 2020)
IISERP-MOF	4-step VSA with LPP	95–90	0.86	1.42	(Burns et al., 2020)
Zeolite NaA	4-step VSA with LPP	95–90	0.9	1.25	(Burns et al., 2020)
Zeolite 13X	4-step VSA with LPP	95–70	0.4	1.4	(Maruyama et al., 2020)
UTSA-16	4-step VSA with LPP	95–70	0.34	1.65	(Maruyama et al., 2020)
Amino silane/Silica	6-step VSA	95–70	1.2	0.14	This work
3D printed amino silane silica	6-step VSA	95–70	1.1	0.33	This work
3D printed UTSA-16	6-step VSA	95–70	0.69	0.89	This work

evacuation steps and therefore the latter approach is recommended for performing process simulations.

The amino silane sorbent had a highly nonlinear isotherm which meant that the energy consumption was higher than the other adsorbents studied in this work. An electrical energy of 1.06 MJ/kg translates to 4.2 MJ/kg on a thermal basis. Such a value is higher than the absorption process using mono-ethanol amine (MEA) and new solvents are being developed that can capture CO_2 at lower energy consumption than MEA (Singh and Stéphenne, 2014). Moreover, these adsorbents are known have thermal stability issues in the presence of oxygen (Bollini et al., 2011). Therefore, one may look for alternative sorbents in the context of post-combustion CO_2 capture from coal fired power plants by VSA processes.

Declaration of Competing Interest

The authors declare that they have no known competing financial interests or personal relationships that could have appeared to influence the work reported in this paper.

Acknowledgement

Appendix A. Supplementary material

Supplementary data to this article can be found online at https://doi.org/10.1016/j.ces.2022.117585.

References

Bollini, P., Choi, S., Drese, J.H., Jones, C.W., 2011. Oxidative Degradation of Aminosilica Adsorbents Relevant to Postcombustion CO_2 Capture. Energy Fuels 25 (5), 2416–2425.

Burns, T.D., Pai, K.N., Subraveti, S.G., Collins, S.P., Krykunov, M., Rajendran, A., Woo, T.K., 2020. Prediction of MOF Performance in Vacuum Swing Adsorption Systems for Postcombustion CO_2 Capture Based on Integrated Molecular Simulations, Process Optimizations, and Machine Learning Models. Environ. Sci. Technol. 54 (7), 4536–4544.

Chaparro-Garnica, C.Y., Jordá-Faus, P., Bailón-García, E., Ocampo-Pérez, R., Aguilar-Madera, C.G., Davó-Quiñonero, A., Lozano-Castelló, D., Bueno-López, A., 2020. Customizable Heterogeneous Catalysts: Nonchanneled Advanced Monolithic Supports Manufactured by 3D-Printing for Improved Active Phase Coating Performance. ACS Appl. Mater. Interfaces 12 (49), 54573–54584.

Couck, S., Cousin-Saint-Remi, J., Van der Perre, S., Baron, G.V., Minas, C., Ruch, P., Denayer, J.F.M., 2018. 3D-printed SAPO-34 monoliths for gas separation. Micropor. Mesopor. Mater. 255, 185–191.

Da Silva, F.A., Silva, J.A., Rodrigues, A.E., 1999. A General Package for the Simulation of Cyclic Adsorption Processes. Adsorption 5, 229–244.

Dhoke, C., Zaabout, A., Cloete, S., Amini, S., 2021. Review on Reactor Configurations for Adsorption-Based CO_2 Capture. Ind. Eng. Chem. Res. 60 (10), 3779–3798.

Farmahini, A.H., Krishnamurthy, S., Friedrich, D., Brandani, S., Sarkisov, L., 2018. From Crystal to Adsorption Column: Challenges in Multiscale Computational Screening of Materials for Adsorption Separation Processes. Ind. Eng. Chem. Res. 57 (45), 15491–15511.

Farmahini, A.H., Krishnamurthy, S., Friedrich, D., Brandani, S., Sarkisov, L., 2021. Performance-Based Screening of Porous Materials for Carbon Capture. Chem. Rev. 121 (17), 10666–10741.

Fiandaca, G., Fraga, E.S., Brandani, S., 2009. A multi-objective genetic algorithm for the design of pressure swing adsorption. Eng. Optim. 41 (9), 833–854.

Grande, C.A., Blom, R., Middelkoop, V., Matras, D., Vamvakeros, A., Jacques, S.D.M., Beale, A.M., Di Michiel, M., Anne Andreassen, K., Bouzga, A.M., 2020. Multiscale investigation of adsorption properties of novel 3D printed UTSA-16 structures. Chem. Eng. J. 402, 126166.

Grande, C.A., Cavenati, S., Barcia, P., Hammer, J., Fritz, H.G., Rodrigues, A.E., 2006. Adsorption of propane and propylene in zeolite 4A honeycomb monolith. Chem. Eng. Sci. 61 (10), 3053–3067.

Haghpanah, R., Nilam, R., Rajendran, A., Farooq, S., Karimi, I.A., 2013. Cycle synthesis and optimization of a VSA process for postcombustion CO_2 capture. AIChE J. 59 (12), 4735–4748.

Hu, Z., Wang, Y., Shah, B.B., Zhao, D., 2019. CO_2 Capture in Metal-Organic Framework Adsorbents: An Engineering Perspective. Adv. Sustain. Syst. 3 (1), 1800080.

IPCC, 2018. IPCC, 2018: Global Warming of 1.5°C. An IPCC Special Report on the impacts of global warming of 1.5°C above pre-industrial levels and related global greenhouse gas emission pathways, in the context of strengthening the global response to the threat of climate change, sustainable development, and efforts to eradicate poverty. In: Masson-Delmotte, V., Zhai, P., Pörtner, H.-O., Roberts, D., Skea, J., Shukla, P.R., Pirani, A., Moufouma-Okia, W., Péan, C., Pidcock, R., Connors, S., Matthews, J.B.R., Chen, Y., Zhou, X., Gomis, M.I., Lonnoy, E., Maycock, T., Tignor, M., Waterfield, T. (Ed.).

Jiang, H., Ebner, A.D., Ritter, J.A., 2020. Importance of Incorporating a Vacuum Pump Performance Curve in Dynamic Adsorption Process Simulation. Ind. Eng. Chem. Res. 59 (2), 856–873.

Khurana, M., Farooq, S., 2016. Simulation and optimization of a 6-step dual-reflux VSA cycle for post-combustion CO_2 capture. Chem. Eng. Sci. 152, 507–515.

Khurana, M., Farooq, S., 2019. Integrated Adsorbent Process Optimization for Minimum Cost of Electricity Including Carbon Capture by a VSA Process. AIChE J. 65 (1), 184–195.

Kiani, A., Jiang, K., Feron, P., 2020. Techno-Economic Assessment for CO_2 Capture from Air Using a Conventional Liquid-Based Absorption Process. Front. Energy Res. 8.

Krishnamurthy, S., Blom, R., Andreassen, K.A., Middelkoop, V., Rombouts, M., Borras, A.B., 2021a. 3D Printed PEI Containing Adsorbents Supported by Carbon Nanostructures for Post-combustion Carbon Capture From Biomass Fired Power Plants. Front. Climate 3.

Krishnamurthy, S., Lind, A., Bouzga, A., Pierchala, J., Blom, R., 2021b. Post combustion carbon capture with supported amine sorbents: From adsorbent characterization to process simulation and optimization. Chem. Eng. J. 406, 127121.

Krishnamurthy, S., Rao, V.R., Guntuka, S., Sharratt, P., Haghpanah, R., Rajendran, A., Amanullah, M., Karimi, I.A., Farooq, S., 2014. CO_2 capture from dry flue gas by vacuum swing adsorption: A pilot plant study. AIChE J. 60 (5), 1830–1842.

Lawson, S., Li, X., Thakkar, H., Rownaghi, A.A., Rezaei, F., 2021. Recent Advances in 3D Printing of Structured Materials for Adsorption and Catalysis Applications. Chem. Rev. 121 (10), 6246–6291.

Lei, L., Bai, L.u., Lindbråthen, A., Pan, F., Zhang, X., He, X., 2020. Carbon membranes for CO_2 removal: Status and perspectives from materials to processes. Chem. Eng. J. 401, 126084.

Liu, M., Nothling, M.D., Webley, P.A., Jin, J., Fu, Q., Qiao, G.G., 2020. High-throughput CO_2 capture using PIM-1@MOF based thin film composite membranes. Chem. Eng. J. 396, 125328.

Lively, R.P., Chance, R.R., Kelley, B.T., Deckman, H.W., Drese, J.H., Jones, C.W., Koros, W.J., 2009. Hollow Fiber Adsorbents for CO_2 Removal from Flue Gas. Ind. Eng. Chem. Res. 48 (15), 7314–7324.

Maruyama, R.T., Pai, K.N., Subraveti, S.G., Rajendran, A., 2020. Improving the performance of vacuum swing adsorption based CO_2 capture under reduced recovery requirements. Int. J. Greenhouse Gas Control 93, 102902.

Mendes, D.N.D.L., Gaspar, A., Ferreira, I., Mota, J.P.B., Ribeiro, R.P.P.L., 2021. 3D-printed hybrid zeolitic/carbonaceous electrically conductive adsorbent structures. Chem. Eng. Res. Des. 174, 442–453.

Middelkoop, V., Coenen, K., Schalck, J., Van Sint Annaland, M., Gallucci, F., 2019. 3D printed versus spherical adsorbents for gas sweetening. Chem. Eng. J. 357, 309–319.

Mohammadi, N., 2017. CO_2 Capture From Flue Gas By A PSA Process Using A Novel Structured Adsorbent, PhD Thesis, College of Engineering and Computing. University of South Carolina.

Nalaparaju, A., Khurana, M., Farooq, S., Karimi, I.A., Jiang, J.W., 2015. CO_2 capture in cation-exchanged metal–organic frameworks: Holistic modeling from molecular simulation to process optimization. Chem. Eng. Sci. 124, 70–78.

Patton, A., Crittenden, B.D., Perera, S.P., 2004. Use of the Linear Driving Force Approximation to Guide the Design of Monolithic Adsorbents. Chem. Eng. Res. Des. 82 (8), 999–1009.

Plaza, M.G., Rubiera, F., Pevida, C., 2017. Evaluating the Feasibility of a TSA Process Based on Steam Stripping in Combination with Structured Carbon Adsorbents To Capture CO_2 from a Coal Power Plant. Energy Fuels 31 (9), 9760–9775.

Rajagopalan, A.K., Avila, A.M., Rajendran, A., 2016. Do adsorbent screening metrics predict process performance? A process optimisation based study for post-combustion capture of CO_2. Int. J. Greenhouse Gas Control 46, 76–85.

Regufe, M.J., Ferreira, A.F.P., Loureiro, J.M., Rodrigues, A., Ribeiro, A.M., 2019. Electrical conductive 3D-printed monolith adsorbent for CO_2 capture. Micropor. Mesopor. Mater. 278, 403–413.

Regufe, M.J., Ferreira, A.F.P., Loureiro, J.M., Shi, Y., Rodrigues, A., Ribeiro, A.M., 2018. New hybrid composite honeycomb monolith with 13X zeolite and activated carbon for CO_2 capture. Adsorption 24 (3), 249–265.

Rezaei, F., Mosca, A., Webley, P., Hedlund, J., Xiao, P., 2010. Comparison of Traditional and Structured Adsorbents for CO_2 Separation by Vacuum-Swing Adsorption. Ind. Eng. Chem. Res. 49 (10), 4832–4841.

Rezaei, F., Webley, P., 2010. Structured adsorbents in gas separation processes. Sep. Purif. Technol. 70 (3), 243–256.

Ruthven, D.M., Thaeron, C., 1997. Performance of a parallel passage adsorbent contactor. Sep. Purif. Technol. 12 (1), 43–60.

Sakwa-Novak, M.A., Yoo, C.-J., Tan, S., Rashidi, F., Jones, C.W., 2016. Poly (ethylenimine)-Functionalized Monolithic Alumina Honeycomb Adsorbents for CO_2 Capture from Air. ChemSusChem 9 (14), 1859–1868.

Sharma, I., Friedrich, D., Golden, T., Brandani, S., 2020. Monolithic Adsorbent-Based Rapid-Cycle Vacuum Pressure Swing Adsorption Process for Carbon Capture from Small-Scale Steam Methane Reforming. Ind. Eng. Chem. Res. 59 (15), 7109–7120.

Singh, A., Stéphenne, K., 2014. Shell Cansolv CO_2 capture technology: Achievement from First Commercial Plant. Energy Proc. 63, 1678–1685.

Sluijter, S.N., Boon, J., James, J., Krishnamurthy, S., Lind, A., Blom, R., Andreassen, K. A., Cormos, A.M., Sandu, V.C., de Boer, R., 2021. 3D-printing of adsorbents for increased productivity in carbon capture applications (3D-CAPS). Int. J. Greenhouse Gas Control 112, 103512.

Subraveti, S.G., Roussanaly, S., Anantharaman, R., Riboldi, L., Rajendran, A., 2021. Techno-economic assessment of optimised vacuum swing adsorption for post-combustion CO_2 capture from steam-methane reformer flue gas. Sep. Purif. Technol. 256, 117832.

Thakkar, H., Eastman, S., Al-Mamoori, A., Hajari, A., Rownaghi, A.A., Rezaei, F., 2017. Formulation of Aminosilica Adsorbents into 3D-Printed Monoliths and Evaluation of Their CO_2 Capture Performance. ACS Appl. Mater. Interfaces 9 (8), 7489–7498.

van der Jagt, R., Vasileiadis, A., Veldhuizen, H., Shao, P., Feng, X., Ganapathy, S., Habisreutinger, N.C., van der Veen, M.A., Wang, C., Wagemaker, M., van der Zwaag, S., Nagai, A., 2021. Synthesis and Structure-Property Relationships of Polyimide Covalent Organic Frameworks for Carbon Dioxide Capture and (Aqueous) Sodium-Ion Batteries. Chem. Mater. 33 (3), 818–833.

Wanderley, R.R., Pinto, D.D.D., Knuutila, H.K., 2020. Investigating opportunities for water-lean solvents in CO_2 capture: VLE and heat of absorption in water-lean solvents containing MEA. Sep. Purif. Technol. 231, 115883.

Wu, J., Zhu, X., Yang, F., Ge, T., Wang, R., 2021. Easily-synthesized and low-cost amine-functionalized silica sol-coated structured adsorbents for CO_2 capture. Chem. Eng. J. 425, 131409.

Yang, L., Shi, C., Li, L., Li, Y.i., 2020. High-throughput model-building and screening of zeolitic imidazolate frameworks for CO_2 capture from flue gas. Chin. Chem. Lett. 31 (1), 227–230.

Zhao, Q., Wu, F., Men, Y., Fang, X., Zhao, J., Xiao, P., Webley, P.A., Grande, C.A., 2019. CO_2 capture using a novel hybrid monolith (H-ZSM5/activated carbon) as adsorbent by combined vacuum and electric swing adsorption (VESA). Chem. Eng. J. 358, 707–717.